POLITECNICO DI TORINO
Repository ISTITUZIONALE

A simplified approach to hydraulic fracturing of rocks based on Finite Fracture Mechanics

(Article begins on next page)

09 May 2024

SPECIAL ISSUE ARTICLE

A simplified approach to hydraulic fracturing of rocks based on Finite Fracture Mechanics

A. Sapora[1] | A. Spagnoli[2] | L. Susmel[3] | P. Cornetti[1]

[1]Department of Structural, Building and Geotechnical Engineering, Politecnico di Torino, Torino, Italy

[2]Department of Engineering and Architecture, University of Parma, Parma, Italy

[3]Department of Civil and Structural Engineering, The University of Sheffield, Sheffield, UK

Correspondence

A. Sapora, Department of Structural, Building and Geotechnical Engineering, Politecnico di Torino, Corso Duca degli Abruzzi 24, 10129 Torino, Italy.
Email: alberto.sapora@polito.it

Abstract

This work presents a coupled approach, based on Finite Fracture Mechanics (FFM), to preliminarily investigate hydraulic fracturing of rocks. The novelty of the criterion relies on the assumption of a finite crack extension and on the simultaneous fulfillment of a stress requirement and the energy balance. Two material constants are involved, namely, the tensile strength and the fracture toughness. The FFM unknowns are represented by the critical crack advance, which results a structural parameter and not a simple material one, and the breakdown pressure. The study investigates the longitudinal failure behavior of both impermeable and permeable rocks by supposing that growing cracks are loaded by a pressure proportional to that acting on the borehole wall. The stability growth of hydraulic fractures is discussed case by case. The approach is validated against experimental data available in the literature by considering the effect of rock permeability, fluid viscosity and flow rate.

KEYWORDS

breakdown pressure, crack advance, energy balance, FFM, longitudinal hydraulic fracture

Highlights

- The FFM criterion is applied to preliminarily assess hydraulic fracturing in rocks.
- The pressure of the penetrating fluid is assumed to be constant around the borehole.
- The breakdown pressure is governed by a competition between strength and toughness.
- It is reasonable to suppose that the crack onset is stable for nonpenetrating fluids.

1 | INTRODUCTION

Hydraulic fracturing (or fracking) is a common technique for productivity enhancement in conventional oil and gas reservoirs by inducing high-conductivity fractures from reservoir to wellbore. Since hydraulic fracturing has become increasingly strategic, the importance of factors effecting tensile crack development in rock

subjected to fluid pressures needs to be thoroughly understood.

Several theoretical, numerical, and experimental analyses have been carried out to evaluate the break-down pressure in different rock types, under different in situ conditions with different fracturing fluids.[1–3] The process is extremely complex, since it is dependent on several factors[4,5] such as in situ horizontal stresses, pressure rate,[6] rock mass properties,[7] fracture-fluid properties,[8] and wellbore size and orientation.[9]

An interesting overview of the most important studies in this framework has been recently presented.[10] Accordingly, common theoretical approaches can be classified into strength-based, energy release rate-based, stress intensity factor-based, or shear failure criteria.

In their pioneering work, Hubbert and Willis[11] developed in 1957 the first realistic model relating the hydraulic fracturing test variables to the in situ state of stress in rock. The approach is based on the simple concept of stress concentration at the borehole edge. Haimson and Fairhurst[12] improved the criterion in 1967 by taking Biot's poroelastic theory into account. However, the model still assumes that the breakdown occurs at a point on the wellbore wall. Therefore, the actual fluid pressure distribution—depending on many factors as outline above—is neglected. In order to overcome this drawback, criteria based on a critical length were then devised and somehow validated. Particularly, the point stress method proposed by Ito and Hayashi[6] assumes that break-down occurs when the maximum effective stress reaches the rock tensile strength at a certain distance (inside the rock mass) from the wellbore surface. The critical distance is assumed to be a material parameter, function of the tensile strength itself and of the rock fracture toughness. Similar nonlocal criteria were successively proposed, based on the average normal stress[7] or on the stress intensity factor function.[13] On the other hand, laying on a number of basic assumptions, shear-based approaches were seen to be oversimplified and therefore unable to provide accurate results.[10]

The body of knowledge briefly described above recalls, on a methodological level, what happened in the framework of fracture mechanics of homogenous materials. Basically, the theory of critical distances (TCD)[14,15] was proposed to overcome the limits of linear elastic fracture mechanics (LEFM) in assessing the failure behavior of notched elements under either static or fatigue loading. In some cases, however, the idea of a length that is a material property is characterized by some drawbacks.[16,17] In this setting, the Finite Fracture Mechanics (FFM) approach[16,18] provides a convincing alternative suitable for overcoming the above limitations. FFM works by coupling a stress condition with the energy

balance, and it involves a structural length, dependent on the geometrical parameters and the loading conditions too. This allows, for instance, a better description of the failure size effect on plain, cracked, or notched structures at small scales. In this framework, the FFM criterion has recently been applied to circular holes under different far field loading conditions[19–21] and under internal pressure for nonpenetrating fluids.[22,23]

The novelty of the present paper is the extension of FFM to fracking by focusing on longitudinal fracture (taking place when the out-of-plane stress results the maximum compressive principal stress) and considering both nonpenetrating and penetrating fluids. To this end, some simplifying assumptions are made as follows: (i) The rock is treated as a linear, elastic, isotropic, and homogeneous medium; (ii) the pressure of the penetrating fluid is assumed to be constant around the hole; (iii) the effect of propagation is described by a unique dimensionless parameter λ ranging from 0 to 1.

This approach will be devised, discussed, and validated in what follows.

2 | FINITE FRACTURE MECHANICS

Let us consider the borehole geometry seen in Figure 1 that consists of a circular hole with radius R in an infinite plate, subjected to internal pressure p and remote compressive loading σ. The reference system of coordinates xy is fixed at the hole center. As it will be clarified at the end of the section, the two parameters α and λ are used to model the loading conditions and the fluid penetration, respectively.
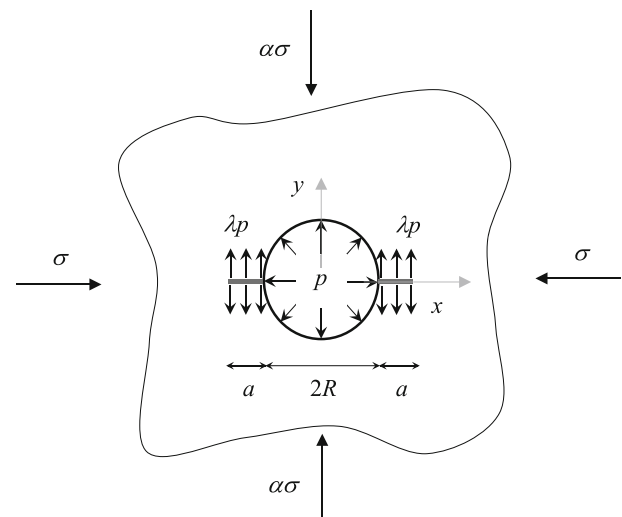

FIGURE 1 Borehole geometry.

The coupled criterion based on FFM[16,24] makes use of a finite crack advance of length l (at least at the initiation stage) and of the simultaneous fulfillment of the following two conditions. The first consists of a stress requirement, according to which the average normal stress σ_y in front of the hole edge must be greater than the tensile strength, T:

$$\widehat{\sigma}(\bar{l}) = \frac{1}{\bar{l}} \int_1^{1+\bar{l}} \sigma_y(\bar{x}) d\bar{x} \geq T \tag{1}$$

where $\bar{l} = l/R$ and $\bar{x} = x/R$.

The second is represented by the energy balance: The average energy release rate G must be greater than the fracture energy G_c. Via Irwin's relationship, this condition can be expressed in terms of stress intensity factor (SIF) K_I ($G = K_I^2/E'$, E' being Young's modulus related to plane strain conditions) and fracture toughness K_{Ic} ($G_c = K_{Ic}^2/E'$) as

$$\widehat{K}(\bar{l}) = \sqrt{\frac{1}{\bar{l}} \int_0^{\bar{l}} K_I^2(\bar{a}) d\bar{a}} \geq K_{Ic} \tag{2}$$

where a is the length of a crack emanating from the hole edge and $\bar{a} = a/R$. Herein, it is supposed that the crack propagates symmetrically along the x-direction, as done in conventional theoretical approaches to hydraulic fracturing.[10,13,25] Note that symmetrical crack propagation has to be preferred—from an energetic point of view—when dealing with mode I crack initiation from circular holes.[26,27]

In order to implement the FFM approach via Equations (1) and (2), the distribution along the line of potential crack growth of the stress field σ_y and of the SIF K_I need to be known, either analytically (through some approximating expressions) or numerically (e.g., through a finite element analysis). In the framework of linear elasticity, both functions are the sum of two contributions, one due to the internal pressure p (which is the sum of the hydraulic pressure and the initial pore pressure) and one due to the remote compressive loading σ. Accordingly, by referring to the geometry under consideration (Figure 1), we have[28]

$$\sigma_y(\bar{x}) = f_\lambda(\bar{x})p + f_\alpha(\bar{x})\sigma \tag{3a}$$

where

$$f_\lambda(\bar{x}) = \left(\lambda + \frac{1}{\bar{x}^2}\right) \tag{3b}$$

and

$$f_\alpha(\bar{x}) = \frac{1}{2}\left[-2\alpha - \frac{(1+\alpha)}{\bar{x}^2} + \frac{3(1-\alpha)}{\bar{x}^4}\right] \tag{3c}$$

The maximum normal stress at the hole edge thus writes as

$$\sigma_y(\bar{x}=1) = \sigma_{\max} = (1+\lambda)p + (1-3\alpha)\sigma \tag{3d}$$

On the other hand, the SIF can be written in the following form:

$$K_I(\bar{a}) = \sqrt{\pi R \bar{a}}\left[p\, F_\lambda(\bar{a}) + \sigma\, F_\alpha(\bar{a})\right] \tag{4a}$$

Approximating expressions for the shape functions F were proposed in the literature with an accuracy better than 1% for any $\bar{a} = a/R$:[29]

$$F_\lambda(\bar{a}) = (1-\lambda)F_0(\bar{a}) + \lambda F_1(\bar{a}) \tag{4b}$$

with

$$F_0(\bar{a}) = \frac{1}{1+\bar{a}}\left[0.637 + \frac{0.485}{(1+\bar{a})^2} + 0.4\frac{\bar{a}^2}{(1+\bar{a})^3}\right] \tag{4c}$$

$$F_1(\bar{a}) = \left\{1 + \frac{1}{1+\bar{a}}\left[\frac{1}{2} + \frac{0.743}{(1+\bar{a})^2}\right]\right\} \tag{4d}$$

and

$$F_\alpha(\bar{a}) = -F_1(\bar{a}) + (1-\alpha)F_2(\bar{a}) \tag{4e}$$

with

$$F_2(\bar{a}) = \frac{1}{2}\left(3 - \frac{\bar{a}}{1+\bar{a}}\right)\left[1 + 1.243\left(1 - \frac{\bar{a}}{1+\bar{a}}\right)^3\right] \tag{4f}$$

The case $\lambda = 0$ refers to nonpenetrating fluids, whereas the range $0 < \lambda \leq 1$ will be investigated in detail hereinafter to describe the case of penetrating fluids by supposing that the fluid pressure within the borehole is proportional to the fluid pressure within the microcracks. This hypothesis was originally proposed when dealing with experimental tests on granite samples.[2] It may be somehow justified by assuming that the size of the area affected by fluid penetration is approximately equal to the critical crack advance. However, the assumption obviously limits the validity of the proposed model.

It should be underlined that the use of a single parameter λ is simplistic to account for the different aspects affecting fluid penetration. The phenomenon is influenced, in first place, by the permeability of the rock (impermeable rocks, such as granite and marble, present a typical permeability less than 10^{-18} m^2, whereas permeable rocks, such as sandstone, show a permeability generally greater than 10^{-16} m^2). Poroelastic models have been proposed for the last 50 years, by including Biot's coefficient (function of the ratio between matrix and bulk compression coefficients) and Poisson's ratio among the parameters that affect the breakdown pressure. Furthermore, it is well known that the fracturing initiation pressure decreases with the decrease of fracturing fluid viscosity and pressurization rate,[6,25,30] and it depends on the damage and micro-cracks that form near the well when drilling or injecting.[2] Thus, the calibration of λ for FFM application on experimental results needs to be discussed case by case.

On the other hand, parameter α weighs the contribution of the remote loads in the two perpendicular directions: $\alpha = 0$ refers to uniaxial compressive loading, $\alpha = 1$ to isotropic biaxial compression. Note that if $\alpha > 1$, the fracture propagates along the y-axis. Without losing generality, we restrict our analysis to the range $0 \leq \alpha \leq 1$.

By substituting Equations (3a)–(3d) into Equation (1), it is possible to express the stress condition as

$$\frac{(2+\bar{l})\left(-2\alpha\bar{l}^2 - 4\alpha\bar{l} + 1 - 3\alpha\right)}{2(1+\bar{l})^3}\left(\frac{\sigma}{T}\right) + \frac{\lambda\bar{l} + 1 + \lambda}{1+\bar{l}}\left(\frac{p}{T}\right) \geq 1 \tag{5}$$

Furthermore, inserting Equations (4a)–(4f) into the energy balance (1) yields

$$I_{\alpha\alpha}\left(\frac{\sigma}{T}\right)^2 + 2I_{\alpha\lambda}\left(\frac{\sigma}{T}\right)\left(\frac{p}{T}\right) + I_{\lambda\lambda}\left(\frac{p}{T}\right)^2 \geq \frac{\bar{l}}{\pi\, R/l_{ch}} \tag{6}$$

where $l_{ch} = (K_{Ic}/T)^2$ is Irwin's characteristic length of the rock, and analytical expressions for integrals $I_{\alpha\alpha} = \int_0^{\bar{l}} \bar{a}F_\alpha^2(\bar{a})d\bar{a}$, $I_{\alpha\lambda} = \int_0^{\bar{l}} \bar{a}F_\alpha(\bar{a})F_\lambda(\bar{a})d\bar{a}$, and $I_{\lambda\lambda} = \int_0^{\bar{l}} \bar{a}F_\lambda^2(\bar{a})d\bar{a}$ can be achieved, although not easy to be handled.

Summarizing, the coupled criterion based on FFM is expressed by the system of inequalities (5) and (6): The unknowns are represented by the critical advancement of the crack l_c and by the breakdown pressure p_f, which reverts to the initiation pressure in case of stable crack propagation. Of course, p_f is the lowest value of p that satisfies Equations (5) and (6) as l varies.

3 | EFFECT OF THE INNER PRESSURE ($\sigma = 0$)

Let us start by considering the effect of internal pressure alone ($\sigma = 0$), which has been partially dealt with in the FFM literature.[23] From classical linear elasticity, it is well known that (Equations 3a–3d)

$$\frac{p_f}{T} \to \frac{1}{\lambda} \quad \text{as} \quad \frac{R}{l_{ch}} \to 0 \tag{7a}$$

$$\frac{p_f}{T} \to \frac{1}{1+\lambda} \quad \text{as} \quad \frac{R}{l_{ch}} \to \infty \tag{7b}$$

In what follows, we will investigate separately the cases of hydraulic fracture involving penetrating and not penetrating fluids ($\lambda = 0$) according to the FFM approach.

3.1 | Penetrating fluids

Let us start assuming fluid penetration before fracture initiation ($0 < \lambda \leq 1$; Figure 1). As λ is high enough ($\lambda > 0.1$, otherwise the situation is similar to that described in Section 3.2), the geometry is such that the SIF function (2) becomes monotonically increasing (so-called positive geometry) (Figure 2); consequently, unstable crack growth will naturally result. Thus, for penetrating fluids, the initiation pressure coincides with the breakdown pressure and the crack onset takes place when both inequalities (5) and (6) are strictly fulfilled, leading to a system of two equations in two unknowns:
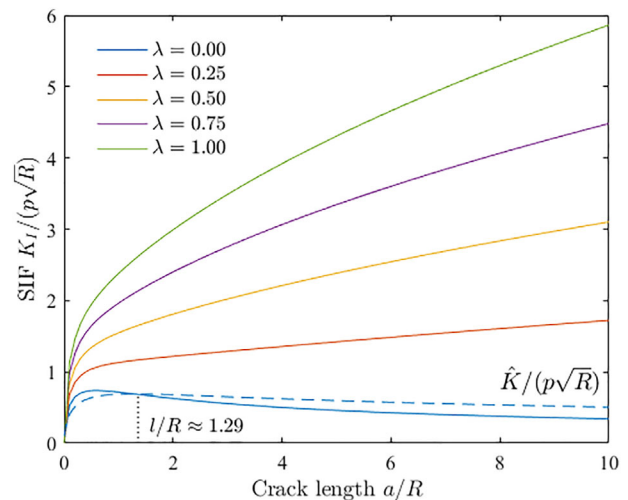

FIGURE 2 Dimensionless SIF as a function of the crack length for λ varying from 0 to 1 ($\sigma = 0$). The dashed line represents the $\widehat{K}$ function (Equation 2) versus l/R for $\lambda = 0$. [Colour figure can be viewed at wileyonlinelibrary.com]
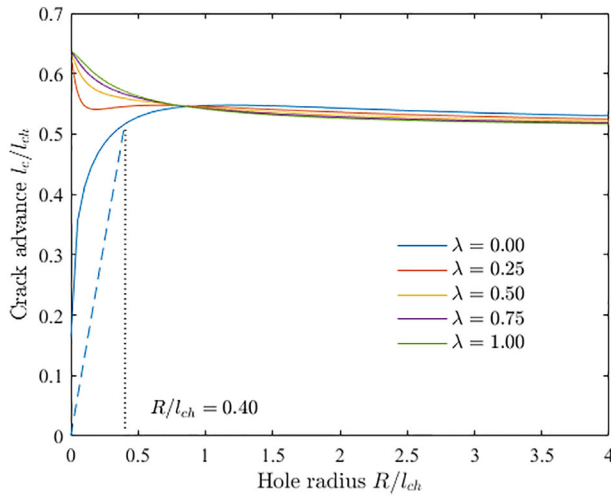
FIGURE 3 FFM ($\sigma = 0$): crack advance according to nonpenetrating fluids ($\lambda = 0$, dashed + continuous blue line) and penetrating fluids ($\lambda > 0.1$, colored lines). [Colour figure can be viewed at wileyonlinelibrary.com]

$$\begin{cases} \dfrac{p}{T} = \dfrac{1+\bar{l}}{\lambda(1+\bar{l})+1} \\[3mm] \dfrac{p}{T} = \sqrt{\dfrac{\bar{l}}{\pi R/l_{ch}} \dfrac{1}{I_{\lambda\lambda}(\bar{l})}} \end{cases} \quad (8)$$

Once the radius R and the material properties l_{ch} are fixed, system (8) can be faced by equaling the right-hand sides of both expressions and solving numerically the implicit equation in l. This allows to get the value of the critical crack advance l_c (first unknown), which can be then substituted into one of the two equations in (8) to get the breakdown pressure p_f (second unknown).

FFM unknowns are depicted in Figures 3 and 4 by considering l_c and p_f, respectively. For a vanishing radius, Equation (7a) holds and the energy balance only provides the crack advance, $l_c/l_{ch} \to 2/\pi \simeq 0.637$. On the other hand, for sufficiently high radii, the breakdown is governed by the stress concentration factor (Equation 7b): Accordingly, $l_c/l_{ch} \to 2/(\pi 1.12^2) \simeq 0.507$. The solution related to intermediate radii is ruled out by both strength and toughness.

3.2 | Nonpenetrating fluids ($\lambda = 0$)

Consider now the case of impermeable rocks ($\lambda = 0$; Figure 1); that is, the fluid is present only in the borehole. Accordingly, the geometry is locally positive and globally negative,[32] since the SIF (4) is first increasing (starting from zero) and then tending again to zero as a tends to
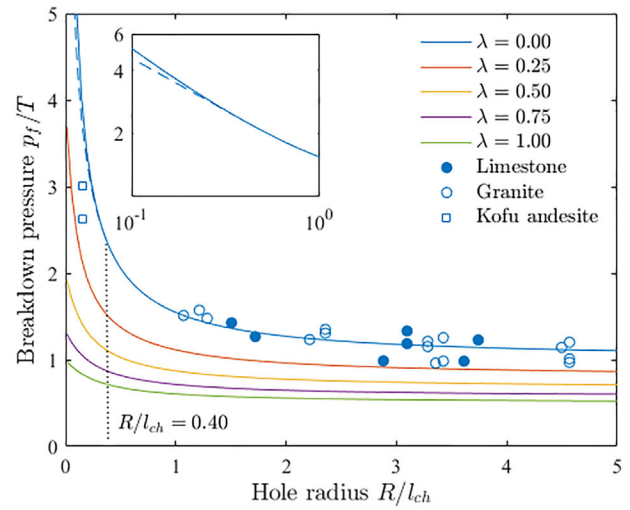

FIGURE 4 FFM ($\sigma = 0$): Breakdown pressure according to nonpenetrating ($\lambda = 0$, stable propagation) and penetrating fluids. The dashed blue line represents the FFM predictions according to Equations (10a) and (10b) for $R/l_{ch} < 0.40$. Experimental data ($\lambda = 0$) are related to limestone[31] (solid circles), granite[31] (empty circles), and Kofu andesite[6] (empty squares). [Colour figure can be viewed at wileyonlinelibrary.com]

infinite (Figure 2). The resulting function $\widehat{K}(\bar{l})$ (Equation 2) attains a maximum at $\bar{l}^* = l/R \simeq 1.29$, from which it follows via Equations (1) and (2):

$$R^* = \frac{R}{l_{ch}} = \frac{\widehat{\sigma}^2(\bar{l}^*)}{1.29\,\widehat{K}(\bar{l}^*)} \simeq 0.40 \quad (9)$$

Two FFM scenarios are now possible (Figure 5) as follows.

Scenario (i): For R/l_{ch} below R^*, the crack onset is provided by the minimum of the discrete energy balance, being the stress requirement (1) trivially (over) fulfilled (Figure 5A).

In formulae:

$$\frac{p_f}{T} = \sqrt{\frac{1.29}{\pi R/l_{ch}} \frac{1}{I_{\lambda\lambda}(\bar{l}^*)}} \simeq \frac{1.45}{\sqrt{R/l_{ch}}} \quad (10a)$$

from which it follows

$$p_f = \frac{1.45}{\sqrt{R}} K_{Ic} \quad (10b)$$

Accordingly, the crack propagation reveals to be stable ($dK_I/da < 0$), and the infinitesimal crack onset at
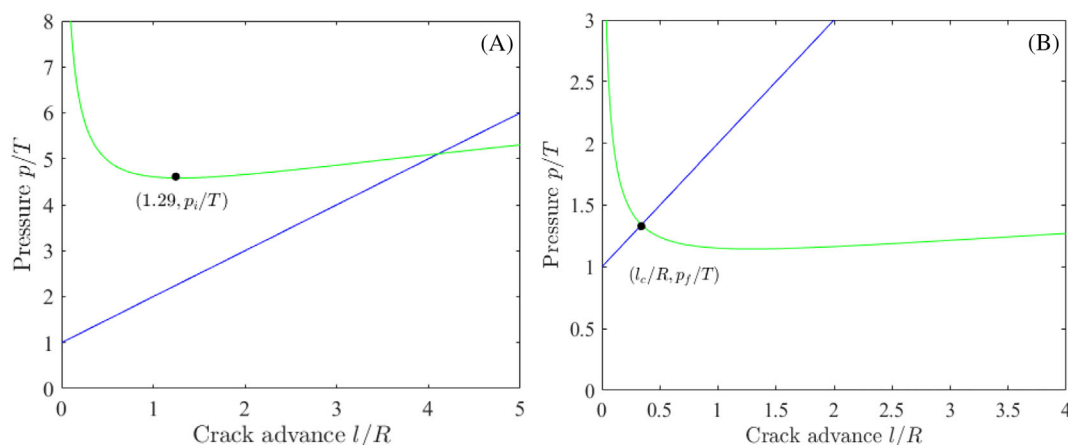
FIGURE 5 Dimensionless pressure ($\sigma = \lambda = 0$) for $R/l_{ch} = 0.1$ (A) and 1.6 (B). FFM solution coincides with the minimum value (black circle) satisfying both the stress requirement (area above the blue line) and the energy balance (area above the green line). [Colour figure can be viewed at wileyonlinelibrary.com]

TABLE 1 Mechanical properties and parameters implemented in the present FFM analysis.

Experimental test	K_{Ic} (MPa$\sqrt{m}$)	T (MPa)	l_{ch} (mm)	λ
Falkenberg granite[2]	1.80	17.0	11.2	0.95
Honkomatsu andesite[6]	1.10	12.1	8.26	0.00
Indiana limestone[31]	0.37[a]	9.60	1.48	0.00
Kofu andesite[6]	1.50	11.1	18.3	0.00
Lac Du Bonnet granite[31]	0.35[a]	8.10	1.87	0.00
Pennant sandstone[34]	0.32	15.1	0.45	0.15–0.35
Strathbogie granite[35]	1.40	6.60	44.9	0.90
Tablerock sandstone[36]	0.55[b]	4.40	15.6	0.50
Whitby mudstone[34]	0.37	3.21	13.3	0.40

[a]Derived from the analysis carried out in the corresponding reference.[31]
[b]Taken from the literature,[30] since it is not provided in the related analysis.

the subsequent steps will be described by LEFM ($K_I = K_{Ic}$): Subsequent increases in pressure are required to cause continued crack propagation. Note that Equations (10a) and (10b) satisfy the limit condition provided by Equation (7a);

Scenario (ii): For R/l_{ch} larger than R^*, the crack onset takes place when both inequalities (5) and (6) are strictly verified (Figure 5B), leading again to system (8) with $\lambda = 0$. The generated cracks could be either unstable or stable, depending on the value of the crack extension[20] (Figure 2).

For nonpenetrating (or slightly penetrating, $\lambda < 0.1$) fluids, in any case, it is reasonable to suppose that the initial growth of the hydraulic cracks is stable because of large pressure drops in the narrow fractures. Subsequent increases in pressure cause however unstable propagation, which correlates with the pressure at which breakdown is observed.

FFM results are presented in Figures 3 and 4, which show the critical crack advance and the initiation pressure, respectively. For sufficiently high R, the solution is stress governed ($p_f/T \to 1$, Equation 7b), and the energy balance only provides the crack advance, $l_c/l_{ch} \to 2/(\pi 1.12^2) \simeq 0.507$.[24] Below R^*, the FFM criterion reverts to Equation (10), and l_c becomes a linear function of R, $l_c = 1.29\,R$.[20,33] Note that, in this range, the deviation from the solution obtained by the coupled system (8) is significant only for the crack extension (Figure 3), the critical pressure being significantly higher only for very small radii (see subplot in Figure 4).

Experimental data taken from the literature and referring to Kofu andesite,[6] Lac du Bonnet granite, and Indiana limestone[31] are also reported in Figure 4. The material properties implemented in the present work are summarized in Table 1: In the case of granite and limestone, the fracture toughness K_{Ic} was extrapolated from

the critical distance used by Cuisiat and Haimson[31] to fit the data through the point method.[6] The global matching between FFM initiation predictions and experimental results is satisfactory.

Finally, let us underline the hole size effect; that is, the failure pressure decreases as the borehole radius increases. This trend will be recovered also in next sections, as it plays a major role in rock fracture mechanics. The behavior is not limited to the presence of a hole but also of common defects such as cracks or notches.[37]

4 | EFFECT OF REMOTE COMPRESSION

In the following, we will analyze separately two additional conditions related to the bore under pressure: Uniaxial ($\alpha = 0$) and isotropic biaxial ($\alpha = 1$) compression; see Figure 1. For each of them, we will comment on the cases of nonpenetrating ($\lambda = 0$) and penetrating ($\lambda = 1$) fluids, comparing FFM predictions with the data available in the literature.

4.1 | Uniaxial compression ($\alpha = 0$)

For a given value of ratio σ/T, from linear elasticity (Equations 3a–3d), we have

$$\frac{p_f}{T} \to \frac{1}{\lambda} \text{ as } \frac{R}{l_{ch}} \to 0 \tag{11a}$$

$$\frac{p_f}{T} \to \frac{1 - \sigma/T}{1 + \lambda} \text{ as } \frac{R}{l_{ch}} \to \infty \tag{11b}$$

The uniaxial compression thus provides a positive contribution to breakdown (at least for sufficiently large radii), the limit by Equation (11b) being lower than that by Equation (7b).

In case of positive geometries, starting from Equations (5) and (6), the FFM system can be rewritten as

$$\begin{cases} \dfrac{p}{T} = \dfrac{1+\bar{l}}{\lambda\bar{l}+1+\lambda} - \dfrac{2+\bar{l}}{2(1+\bar{l})^2(\lambda\bar{l}+1+\lambda)}\dfrac{\sigma}{T} \\[2ex] \dfrac{p}{T} = \dfrac{-\dfrac{\sigma}{T}I_{\alpha\lambda} + \sqrt{\left(\dfrac{\sigma}{T}\right)^2 I_{\alpha\lambda}^2 - \left[\left(\dfrac{\sigma}{T}\right)^2 I_{\lambda\lambda}\left(I_{\alpha\alpha} - \dfrac{\bar{l}}{\pi\,R/l_{ch}}\right)\right]}}{I_{\lambda\lambda}} \end{cases}_{\alpha=0} \tag{12}$$

which can be solved numerically analogously to the procedure described in Section 3.1 (see Equation 8).

By taking $\sigma/T = 0.4$ (each case has to be faced separately), the FFM solutions are reported in Figures 6 and 7 for l_c and p_f, respectively, for different values of λ. Note that the behavior of the l_c versus R relationship is qualitatively similar to that of the pressurized hole (Figure 3).

Indeed, the solution from system (12) can be accepted rigorously only for positive geometries. This is not the case of nonpenetrating fluids ($\lambda = 0$). Accordingly, the geometry is again locally positive and globally negative. The average function $\widehat{K}$ (Equation 2) is reported in Figure 8 for different p/T values ranging from 1 to 5 (note
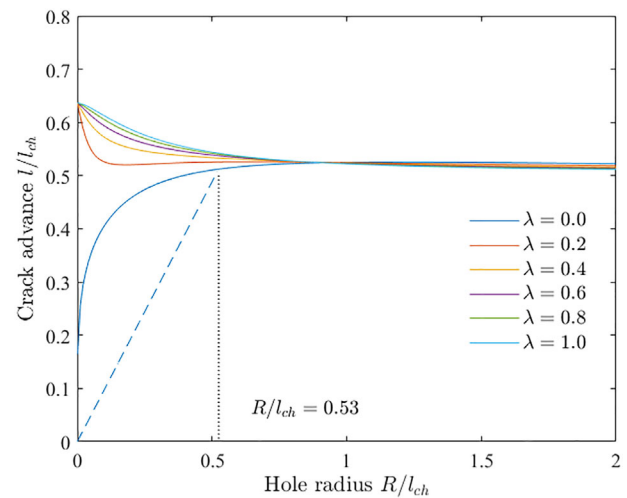

FIGURE 6 FFM ($\alpha = 0$, $\sigma/T = 0.4$): Dimensionless crack advance for different λ values. [Colour figure can be viewed at wileyonlinelibrary.com]
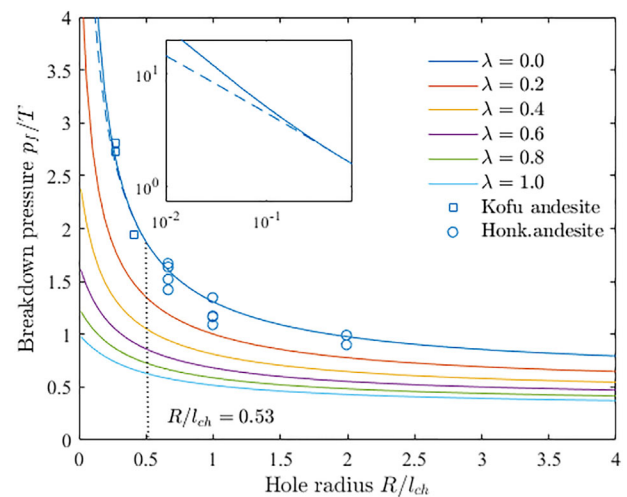

FIGURE 7 FFM ($\alpha = 0$, $\sigma/T = 0.4$): Dimensionless failure pressure for different λ values. The dashed blue line represents the FFM energy solution for $R/l_{ch} < 0.53$ and $\lambda = 0$ (stable propagation). Experimental data[31] (empty symbols) refer to $\lambda = 0$. [Colour figure can be viewed at wileyonlinelibrary.com]

that the function is now plotted in dimensionless form with respect to the tensile strength T). The dashed line in Figure 8 represents the locus of maxima, from which, through a relationship similar to Equation (9), the critical radii versus p/T function can be estimated. Its intersection with the solution of the coupled system (12) —see Figure 7, $\lambda = 0$— provides the critical radius $R^* = 0.53$. Note that this value lies in between those corresponding just to internal pressure, $R^* = 0.40$ (Equation 8), and to compressive loading, $R^* = 1.44$.[20] Consequently, the threshold crack advance can be estimated from Figure 6: $\bar{l}^* = 0.977$. This estimation depends obviously on the loading σ/T at hand.

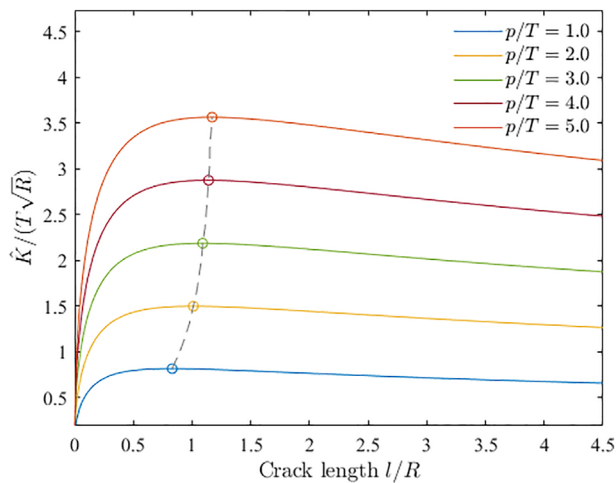The situation is now similar to that described in Section 3.2.

FIGURE 8 Dimensionless $\widehat{K}$ function (Equation 2: $\alpha = 0$, $\sigma/T = 0.4$). Circles represent the maximum of each curve. [Colour figure can be viewed at wileyonlinelibrary.com]
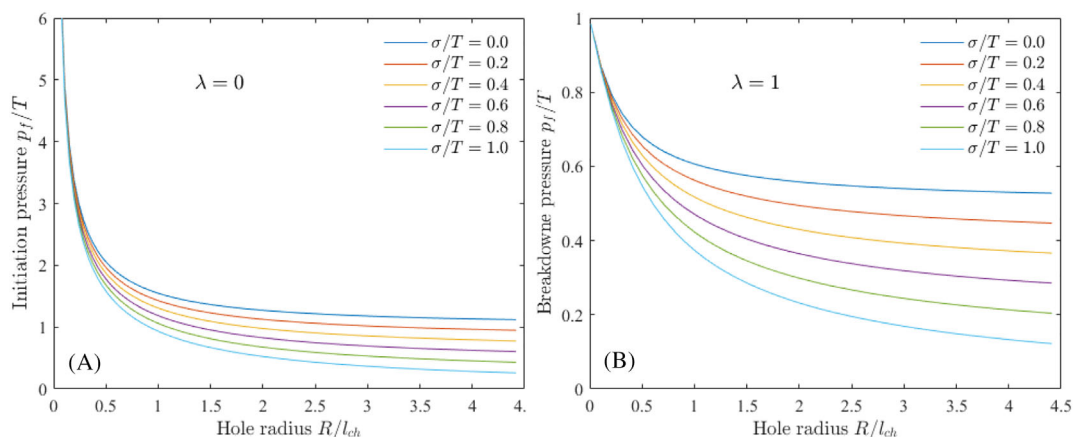
Scenario (i): For R/l_{ch} below R^*, the crack propagation is stable and the onset is provided by the minimum of the discrete energy balance (2) by forcing l/R to equal to 0.977. The subsequent propagation will be stable.

Scenario (ii): For R/l_{ch} larger than R^*, the crack initiation starts when both FFM inequalities are strictly verified, leading to the solution provided by Equation (12) with $\lambda = 0$. Although the propagation may result initially unstable, from a theoretical point of view, it is reasonable to suppose that the initial growth of the hydraulic cracks is stable as discussed after point (ii) of Section 3.2.

Once more, as evident from the subplot of Figure 7, the procedure described in (i) leads to significant deviations in the initiation pressure values only for very small radii.

Experimental data available in the literature are reported in Figure 7. Wellbores were machined in dry cubical specimens and jacketed with an impermeable membrane.[6] Distances among the wellbores and specimen surfaces were kept 10 times larger than the wellbore radius to avoid elastic interactions. Hydraulic tests were carried out under a compressive loading σ equal to 4.91 MPa on two different types of low permeable andesite, namely, Kofu andesite and Honkomatsu andesite, whose material properties[6] are reported in Table 1. Note that the tensile strength values are similar, so that $\sigma/T \approx 0.4$ for both materials. Experimental results refer to the initiation pressure and are in excellent agreement with FFM predictions (Figure 7).

We can now remove the hypothesis of a fixed σ/T and plot the failure pressure as a function of the ratio σ/T, both for $\lambda = 0$ and $\lambda = 1$ (Figure 9). In the former case, FFM prediction are reported disregarding the energy driven solution: Note that R^* can be reasonably supposed to increase as σ/T increases.

FIGURE 9 FFM ($\alpha = 0$): dimensionless failure pressure related to (A) nonpenetrating ($\lambda = 0$) and (B) penetrating ($\lambda = 1$) fluids. [Colour figure can be viewed at wileyonlinelibrary.com]

In Figure 10, we plotted the safety domain for R/l_{ch} equal to 2, 4, and ∞, the last value coinciding with classical linear elasticity along with Rankine criterion. The domain is (weakly) nonlinear according to FFM, the nonlinearity increasing for decreasing R/l_{ch}. This is a consequence of the discrete energy balance (2), which is quadratic in the load.

It is clear that the situation presented above describes the extreme situations of nonpenetrating fluids and penetrating fluids with regard to the crack onset: Note that the initiation pressure always reveals lower in the second case (for a given radius and material), in good agreement with experimental observations.[5]
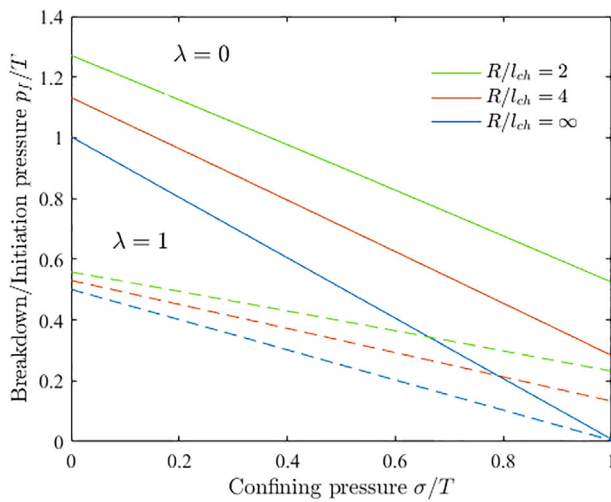
4.2 | Isotropic compression ($\alpha = 1$)

The case of isotropic biaxial compression is more complicated to address than the previous one. This is because the effect of the loading σ is now negative upon the stress field and the SIF in front of the borehole wall. For the sake of simplicity, let us fix again ratio σ/T. From Equations (3a)–(3d), we have

$$\frac{p_f}{T} \to \frac{1+\sigma/T}{\lambda} \quad \text{as} \quad \frac{R}{l_{ch}} \to 0 \tag{13a}$$

$$\frac{p_f}{T} \to \frac{1+2\sigma/T}{1+\lambda} \quad \text{as} \quad \frac{R}{l_{ch}} \to \infty \tag{13b}$$

Note that the limits provided by Equations (13a) and (13b) are higher than the corresponding ones by Equations (11a) and (11b).

Starting from Equations (5) and (6), for positive geometries, the FFM system can be rewritten as

$$\begin{cases} \dfrac{p}{T} = \dfrac{1+\bar{l}}{\lambda\bar{l}+1+\lambda} + \dfrac{2+\bar{l}}{\lambda\bar{l}+1+\lambda}\dfrac{\sigma}{T} \\[2ex] \dfrac{p}{T} = \dfrac{-\frac{\sigma}{T}I_{\alpha\lambda} + \sqrt{\left(\frac{\sigma}{T}\right)^2 I_{\alpha\lambda}^2 - \left[\left(\frac{\sigma}{T}\right)^2 I_{\lambda\lambda}\left(I_{\alpha\alpha} - \frac{\bar{l}}{\pi}\frac{1}{R/l_{ch}}\right)\right]}}{I_{\lambda\lambda}} \Bigg|_{\alpha=1} \end{cases} \tag{14}$$

which can be solved as already discussed (see Equation 8). FFM solutions are plotted in Figure 11A for different λ ($\sigma/T = 0.4$) and in Figure 12 for different σ/T ($\lambda = 1$) values.

FIGURE 10 Safety domains according to FFM ($\alpha = 0$) for both nonpenetrating ($\lambda = 0$, continuous lines: initiation pressure) and penetrating ($\lambda = 1$, dashed lines: breakdown pressure) fluids. [Colour figure can be viewed at wileyonlinelibrary.com]
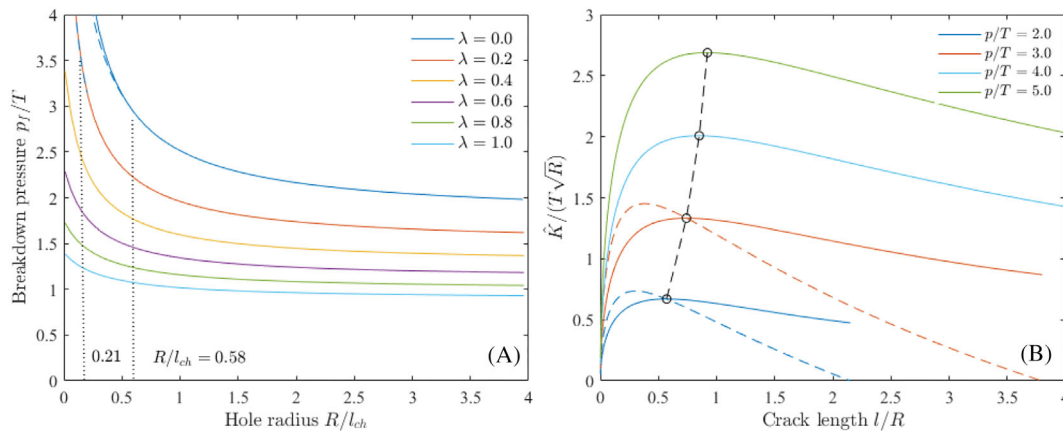
FIGURE 11 (A) FFM ($\alpha = 1$, $\sigma/T = 0.4$): dimensionless breakdown pressure for different λ values; (B) dimensionless $\widehat{K}$ function (Equation 2) for $\lambda = 0$. Circles represent the maximum of each curve. The dashed lines represent the SIFs (Equation 4) versus a/R. [Colour figure can be viewed at wileyonlinelibrary.com]
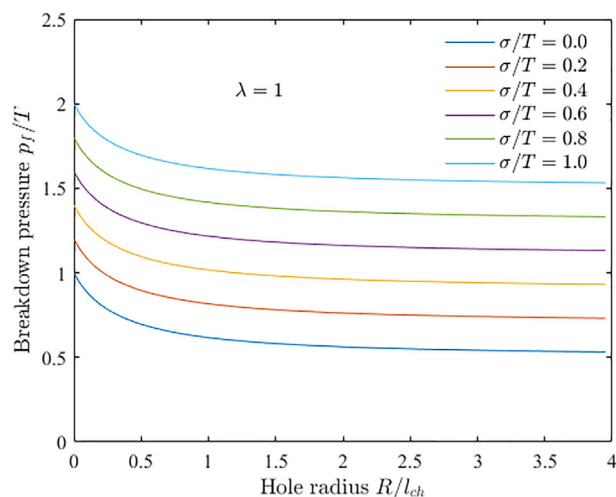
FIGURE 12 FFM ($\alpha = 1$): dimensionless breakdown pressure for $\lambda = 1$. [Colour figure can be viewed at wileyonlinelibrary.com]
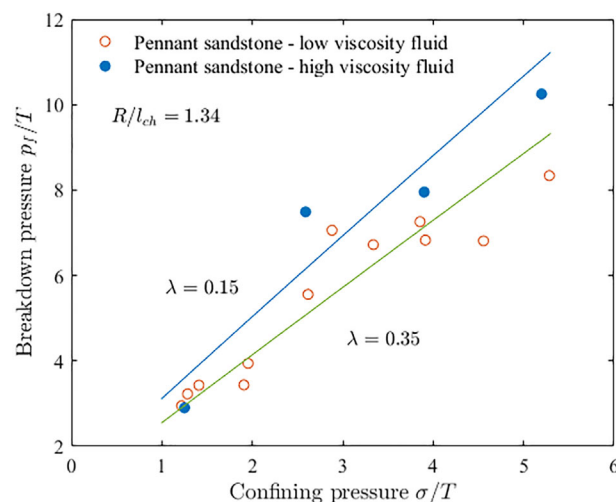

FIGURE 13 FFM ($\alpha = 1$) dimensionless breakdown pressure vs. experimental data referring to Pennant sandstone.[34] Results refer to low viscosity (green) and high viscosity (blue) injected fluid. [Colour figure can be viewed at wileyonlinelibrary.com]

On the other hand, for negative geometries, one has to check first of all the sign of the SIF and the stress field. Due to the high number of parameters, let us set again σ/T equal to 0.4 (each situation has to be investigated separately). Equation (2) is plotted in Figure 11B for different p/T values. The geometry is again globally negative. Furthermore, for low p/T, the SIF vanishes at a specific length and then becomes negative. Basically, attention has to be paid that the crack onset cannot take place in this case. For $\lambda = 0$, we get a critical radius $R^* = 0.58$ ($\bar{l}^* = 0.86$), which however does not influence consistently the FFM predictions on initiation pressure (Figure 11A). The same applies for $\lambda = 0.2$: $R^* = 0.21$ ($\bar{l}^* = 2.5$).

Finally, we compare FFM predictions with experimental results available in literature[2,34,36] and referring to thick walled hollow cylinders with an external to internal radius ratio comprised between 8 and 20.

The first data set refers to experiments carried out under low volume rate on samples ($R = 0.6$ mm) made of Pennant sandstone.[34] The material has a low permeability (around 10^{-18} m^2), and its mechanical properties were evaluated experimentally (Table 1), resulting in $R/l_{ch} \sim 1.34$. Varying the confining pressure, tests were performed with two different injected fluids, a high viscosity (2×10^3 Pa s) one and a low viscosity (2.4×10^{-2} Pa s) one. In the second case, the recorded breakdown pressures were slightly higher (Figure 13). The comparison with FFM predictions reveals satisfactory by choosing, as a fitting parameter, $\lambda = 0.15$ and 0.35, respectively. Identical tests were carried out with the low viscosity fluid on other rocks with similar permeabilities[34]: Mancos shale, Penrhyn slate, and Whitby mudstone. The FFM fitting involves λ estimations close

to the present one: The comparison with results on mudstone ($R/l_{ch} \sim 0.045$) is reported in Figure 14.

The second data set is related to hydraulic fracturing of Tablerock sandstone.[36] Tests were carried out on unjacketed samples and the fluid viscosity was 2.5 Pa s. The material has a high permeability (10^{-13} m^2), and the mechanical properties are reported in Table 1: note that the fracture toughness was not evaluated in the original work and a typical value for sandstone is implemented.[30] Consequently, since $R = 6.5$ mm, $R/l_{ch} \sim 0.42$. Results are presented in Figure 15: FFM predictions reveal satisfactory by choosing $\lambda = 0.50$. Despite the greater permeability of Tablerock sandstone with respect to that of mudstone, the fluid viscosity (see above) and the pressurization rate (15 MPa s^{-1}) were higher in this test: This justifies a λ value just slightly higher than that obtained for mudstone (Figure 14). It should be mentioned also that, different from previous experimental data, the initial pore pressure in this case was not zero but equal to the confining stress: This behavior is implicitly described by the value estimated for λ. Note that the breakdown pressure is the sum of the hydraulic pressure and the initial pore pressure. Moreover, it is important to mention that, according to classical poroelastic models, the pore pressure affects both the poroelastic contribution to fluid penetration and the strength decrease of the rock.[38]

Let us now consider the hydraulic fracturing experiments on Strathbogie granite.[35] The material has a low permeability (10^{-18} m^2). Considering that R was equal 1.5 mm and implementing the mechanical properties reported in Table 1 (again a typical value for the fracture toughness is taken into account, since not reported in the
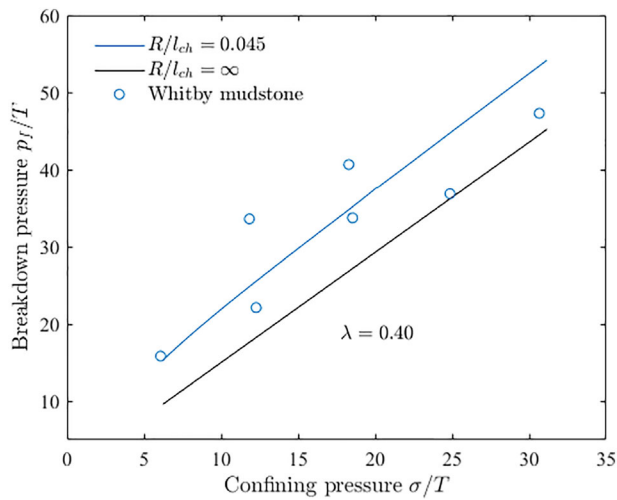
FIGURE 14 FFM ($\alpha = 1$) dimensionless breakdown pressure vs. experimental data referring to referring to Whitby mudstone.[34] The black line refers to classical linear elasticity, Equation (13b). [Colour figure can be viewed at wileyonlinelibrary.com]
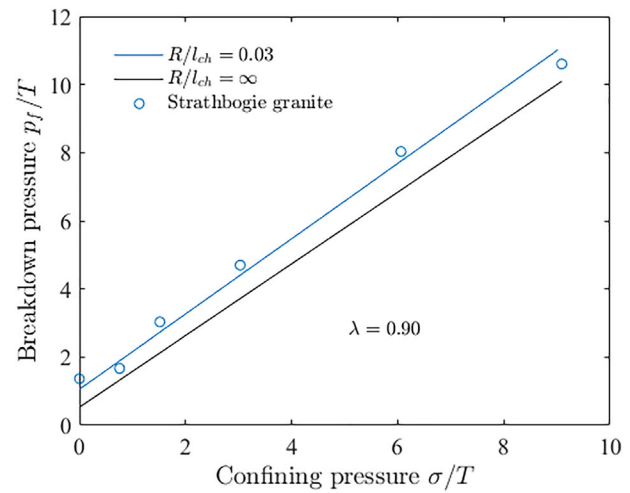

FIGURE 16 FFM ($\alpha = 1$) dimensionless breakdown pressure versus experimental data on Falkenberg granite.[2] The black line refers to classical linear elasticity, Equation (13b). [Colour figure can be viewed at wileyonlinelibrary.com]

FIGURE 15 FFM ($\alpha = 1$) dimensionless breakdown pressure versus experimental data referring to Tablerock sandstone.[36] The black line refers to classical linear elasticity, Equation (13b). [Colour figure can be viewed at wileyonlinelibrary.com]

FIGURE 17 FFM ($\alpha = 1$) dimensionless breakdown pressure vs. experimental data on Falkenberg granite.[2] The black line refers to classical linear elasticity, Equation (13b). [Colour figure can be viewed at wileyonlinelibrary.com]
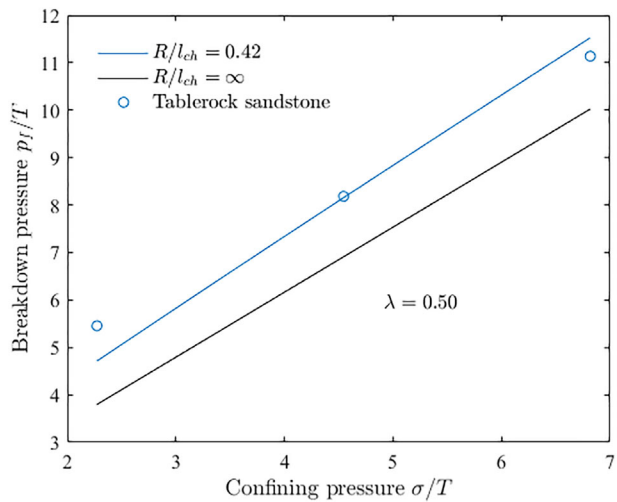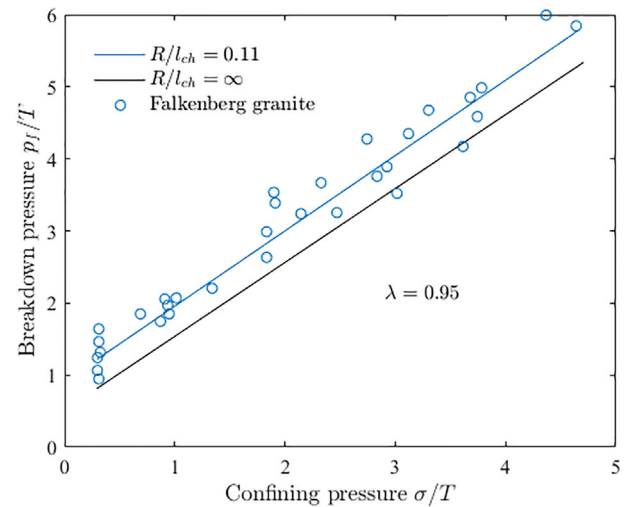
corresponding reference), it follows that $R/l_{ch} \sim 0.03$. FFM predictions match experimental data by implementing $\lambda = 0.9$ (Figure 16): This can be justified by considering the low viscosity of the water (~ 0.9 Pa s) as injection fluid. The fluid flow rate was 5 mL/min. Note that similar results are obtained for tests on Harcourt granite presented in the same analysis.[35]

Finally, the last considered data set refers to hydrofracture tests carried out on Falkenberg granite minicores[2] ($R = 1.25$ mm, $R/l_{ch} \sim 0.11$). The permeability of granite

was low (10^{-18} m²), as well as the viscosity of the injected oil and the pumping rate (0.5 MPa s⁻¹). The existence of pre-existing microdefects was underlined before failure, whereas symmetrical axial fractures were observed after failure. FFM predictions are seen to be very accurate by setting $\lambda = 0.95$ (Figure 17). This assumption looks reasonable according to what was outlined before. Note that in this case, the hypothesis that the fluid pressure within the borehole is proportional to that within microcracks was put forward in the corresponding reference.[2]

5 | CONCLUSIONS

Different from either stress or energy approaches based on a critical distance,[14] FFM requires the simultaneous fulfillment of a stress requirement and the energy balance.[16,18] Thanks to this peculiarity, the criterion is able to distinguish between unstable and stable crack propagation when passing from strength to toughness-governed failure regimes, as for instance when the characteristic size of the stress-concentrator decreases. In this context, the coupled criterion was preliminarily applied to assess hydraulic fracturing in rock materials. The analysis focused on longitudinal fracture and was based on some simplifying assumptions. In particular, (i) rock is modeled as isotropic and homogeneous and (ii) for penetrating fluids, the area surrounding the borehole is subjected to a pressure proportional to that acting on the borehole wall.

It was shown that, for nonpenetrating fluids ($\lambda = 0$), the crack onset is energy governed below a critical radius R^*, whose value increases as far as additional compressive loading conditions are taken into account. In this region, the crack propagation is seen to be stable. For increasing values of R/l_{ch}, fracturing is governed by both strength and toughness, and, in the limit, it is described by the stress concentration factor. Theoretically, depending on the crack length, the propagation could be initially unstable. Practically, it is reasonable to suppose that the initial growth of hydraulic cracks is stable because of the large pressure drop in fractures with narrow widths. In any case, a subsequent increase in pressure can cause unstable propagation, which correlates with the pressure at which breakdown is observed (thus higher than the corresponding initiation pressure).

For fully penetrating fluids ($\lambda = 1$), there are two significant differences: (i) The breakdown is strength-governed at small size and (ii) the crack propagation always results unstable, independently of the radius.

In situations of practical interest, the pressure in the cracks represents something between the two cases ($0 < \lambda < 1$) and the breakdown is affected by many parameters. Each data set must be then investigated separately. Indeed, FFM failure predictions were compared with some experimental data available in the literature and concerning different rock materials, showing a general good agreement.

We would like to remark that the present approach reveals simplistic to account for different factors affecting fluid penetration through the only parameter λ. Further efforts should be spent to improve it, showing a clear correlation with matrix permeability, pressurization rate, and viscosity, for example, similar to what Zhang et al.[30] proposed.

Future investigation steps include the FFM generalization to anisotropic loading conditions ($\alpha < 1$), which might be applied to fracture on horizontal wells; the extension to transverse fracture[8] (taking place when the out-of-plane stress is the minimum compressive principal stress) by modeling the borehole surface as a Penny-shaped crack[39]; the employment of a pressure distribution inside the rock which reveals more physically sound[10]; and the removal of the material isotropy hypothesis.[7] In this latter case, both the stress field and the SIF depend on orientation,[40] and the FFM approach requires the involvement of the angle between the bedding plane and potential crack advance.

NOMENCLATURE

a	length of a crack at the hole edge
$\overline{a}$	dimensionless crack length with respect to the hole radius R
F_α	shape function related to the SIF for compressive loadings
F_λ	shape function related to the SIF for internal pressure
f_α	shape function related to the stress field for compressive loading
f_λ	shape function related to the stress field for the internal pressure
l	crack advance
$\overline{l}$	dimensionless crack advance with respect to the hole radius R
l_c	critical crack advance
l_{ch}	Irwin's length
G	energy release rate
G_c	fracture energy
p	internal pressure
p_f	breakdown pressure
R	borehole radius
R^*	dimensionless radius corresponding to the maximum of $\widehat{K}$
T	tensile strength
K_I	stress intensity factor
K_{Ic}	fracture toughness
$\widehat{K}$	square root of the averaged energy release rate
α	loading parameter
λ	permeability parameter
σ	remote compressive loading
σ_y	normal stress field
$\widehat{\sigma}$	averaged normal stress field

DATA AVAILABILITY STATEMENT

The data that support the findings of this study are available from the corresponding author upon reasonable request.

ORCID

A. Sapora https://orcid.org/0000-0003-3181-3381
A. Spagnoli https://orcid.org/0000-0002-0592-7003
L. Susmel https://orcid.org/0000-0001-7753-9176

REFERENCES

1. Zoback MD, Rummel F, Jung R, Raleigh CB. Laboratory hydraulic fracturing experiments in intact and pre-fractured rock. *Int J Rock Mech min Sci*. 1977;14(2):49-58.
2. Rummel F. Fracture mechanics approach to hydraulic fracturing stress measurements. In: *Fracture Mechanics of Rock*. Elsevier; 1987:217-240.
3. Schmitt DR, Zoback MD. Infiltration effects in the tensile rupture of thin walled cylinders of glass and granite: implications for the hydraulic fracturing breakdown equation. *Int J Rock Mech min Sci*. 1993;30(3):289-303.
4. Schmitt DR, Currie CA, Zhang L. Crustal stress determination from boreholes and rock cores: fundamental principles. *Tectonophysics*. 2012;580:1-26.
5. Arzuaga-García I, Einstein H. Experimental study of fluid penetration and opening geometry during hydraulic fracturing. *Eng Fract Mech*. 2020;230:106986.
6. Ito T, Hayashi K. Physical background to the breakdown pressure in hydraulic fracturing tectonic stress measurements. *Int J Rock Mech min Sci*. 1991;28(4):285-293.
7. Wang J, Xie H, Li C. Anisotropic failure behaviour and breakdown pressure interpretation of hydraulic fracturing experiments on shale. *Int J Rock Mech min Sci*. 2021;142:104748.
8. Li X, Feng Z, Han G, Elsworth D, Marone C, Saffer DCDS. Breakdown pressure and fracture surface morphology of hydraulic fracturing in shale with H_2O, CO_2 and N_2. *Geomech Geophys Geo-Energy Geo-Resources*. 2016;2(2):63-76.
9. Cuss RJ, Rutter EH, Holloway RF. Experimental observations of the mechanics of borehole failure in porous sandstone. *Int J Rock Mech min Sci*. 2003;40(5):747-761.
10. Sampath KHSM, Perera MSA, Ranjith PG. Theoretical overview of hydraulic fracturing break-down pressure. *J Nat gas Sci Eng*. 2018;58:251-265.
11. Hubbert MK, Willis DG. Mechanics of hydraulic fracturing. *Trans Soc Pet Eng AIME*. 1957;210(1):153-163.
12. Haimson B, Fairhurst C. Initiation and extension of hydraulic fractures in rocks. *Soc Pet Eng J*. 1967;7(3):310-318.
13. Schwartzkopff AK, Melkoumian NS, Xu C. Fracture mechanics approximation to predict the breakdown pressure using the theory of critical distances. *Int J Rock Mech min Sci*. 2017;95:48-61.
14. Taylor D. *The Theory of Critical Distances: A New Perspective in Fracture Mechanics*. Elsevier; 2007.
15. Susmel L. *Multiaxial Notch Fatigue*. Woodhead Publishing Limited; 2009.
16. Cornetti P, Pugno N, Carpinteri A, Taylor D. Finite fracture mechanics: a coupled stress and energy failure criterion. *Eng Fract Mech*. 2006;73(14):2021-2033.
17. Doitrand A, Henry R, Meille S. Brittle material strength and fracture toughness estimation from four-point bending test. *J Theor Comput Appl Mech*. 2021;1-17.
18. Leguillon D. Strength or toughness? A criterion for crack onset at a notch. *Eur J Mech A/Solids*. 2002;21(1):61-72.
19. Rosendahl PL, Weißgraeber P, Stein N, Becker W. Asymmetric crack onset at open-holes under tensile and in-plane bending loading. *Int J Solids Struct*. 2017;113–114:10-23.
20. Sapora A, Cornetti P. Crack onset and propagation stability from a circular hole under biaxial loading. *Int J Fract*. 2018;214(1):97-104.
21. Doitrand A, Sapora A. Nonlinear implementation of Finite Fracture Mechanics: a case study on notched Brazilian disk samples. *Int J Non Linear Mech*. 2020;119:103245.
22. Lecampion B. Modeling size effects associated with tensile fracture initiation from a wellbore. *Int J Rock Mech min Sci*. 2012;56:67-76.
23. Sapora A, Efremidis G, Cornetti P. Non-local criteria for the borehole problem: Gradient Elasticity versus Finite Fracture Mechanics. *Meccanica*. 2022;57(4):871-883.
24. Carpinteri A, Cornetti P, Pugno N, Sapora A, Taylor D. A finite fracture mechanics approach to structures with sharp V-notches. *Eng Fract Mech*. 2008;75(7):1736-1752.
25. Wu F, Li D, Fan X, Liu J, Li X. Analytical interpretation of hydraulic fracturing initiation pressure and breakdown pressure. *J Nat gas Sci Eng*. 2020;76:103185.
26. Sapora A, Torabi AR, Etesam S, Cornetti P. Finite Fracture Mechanics crack initiation from a circular hole. *Fatigue Fract Eng Mater Struct*. 2018;41(7):1627-1636.
27. Suknev SV. Extending the theory of critical distances to quasi-brittle fracture. *Theor Appl Fract Mech*. 2021;114:102996.
28. Kirsch G. Die Theorie der Elastizitat und die Bedurfnisse der Festigkeitslehre. *Zantralblatt Verlin Dtsch Ingenieure*. 1898;42:797-807.
29. Tada H, Paris PC, Irwin GR. *The Stress Analysis of Cracks Handbook*. Third ed; 2010.
30. Zhang X, Wang JG, Gao F, Ju Y. Impact of water, nitrogen and CO_2 fracturing fluids on fracturing initiation pressure and flow pattern in anisotropic shale reservoirs. *J Nat gas Sci Eng*. 2017;45:291-306.
31. Cuisiat FD, Haimson BC. Scale effects in rock mass stress measurements. *Int J Rock Mech min Sci*. 1992;29(2):99-117.
32. Weißgraeber P, Hell S, Becker W. Crack nucleation in negative geometries. *Eng Fract Mech*. 2016;168:93-104.
33. Mantič V. Interface crack onset at a circular cylindrical inclusion under a remote transverse tension. Application of a coupled stress and energy criterion. *Int J Solids Struct*. 2009;46(6):1287-1304.
34. Chandler MR, Mecklenburgh J, Rutter E, Lee P. Fluid injection experiments in shale at elevated confining pressures: determination of flaw sizes from mechanical experiments. *J Geophys Res Solid Earth*. 2019;124(6):5500-5520.
35. Kumari WGP, Ranjith PG, Perera MSA, et al. Hydraulic fracturing under high temperature and pressure conditions with micro CT applications: geothermal energy from hot dry rocks. *Fuel*. 2018;230:138-154.
36. Song I, Suh M, Won KS, Haimson B. A laboratory study of hydraulic fracturing breakdown pressure in tablerock sandstone. *Geosci J*. 2001;5(3):263-271.
37. Ayatollahi MR, Akbardoost J. Size and geometry effects on rock fracture toughness: mode I fracture. *Rock Mech Rock Eng*. 2014;47(2):677-687.

38. Ito T. Effect of pore pressure gradient on fracture initiation in fluid saturated porous media: rock. *Eng Fract Mech*. 2008;75(7): 1753-1762.

39. Cornetti P, Sapora A. Penny-shaped cracks by finite fracture mechanics. *Int J Fract*. 2019;219(1):153-159.

40. Nejati M, Bahrami B, Ayatollahi MR, Driesner T. On the anisotropy of shear fracture toughness in rocks. *Theor Appl Fract Mech*. 2021;113:102946.